Supplementary material

An analytical method for 3-dimensional calculation of the contaminant X-ray dose in water caused by clinical electron-beam irradiation

Akira Iwasaki, Shingo Terashima, Shigenobu Kimura, Kohji Sutoh, Kazuo Kamimura, Yoichiro Hosokawa, and Masanori Miyazawa

http://dx.doi.org/10.14312/2399-8172.2020-2

Appendix A

Datasets for the $Q_a(E)$, $Q_b(E)$, $\beta(E)$, $f_0(E)$, and FAC functions

Figure A1 shows (a) $Q_{\mathrm{a}}(E)$, (b) $Q_{\mathrm{b}}(E)$, (c) $\beta(E)$, and (d) $f_0(E)$ datasets from equations 19-22, respectively, including the corresponding datasets (in dots) yielded using Tables 1(a) and (b); Figure A2 shows how the FAC function of equation 23 varies with $S_{\mathrm{appl}}^{\mathrm{iso}}$ and *E*, but under Case-1 to -16, by comparing with the corresponding data in Tables 1(a) and (b); Figures A3 shows (a) $Q_{\mathrm{a}}(E)$, (b) $Q_{\mathrm{b}}(E)$, (c) $\beta(E)$, and (d) $f_0(E)$ datasets from equations 24-27, respectively, including the corresponding datasets (in dots) yielded from Tables 1(c) and (d). Figure A4 shows how the FAC function of equation 28 varies under Case-17 to -32, by comparing with the corresponding data in Tables 1(c) and (d).

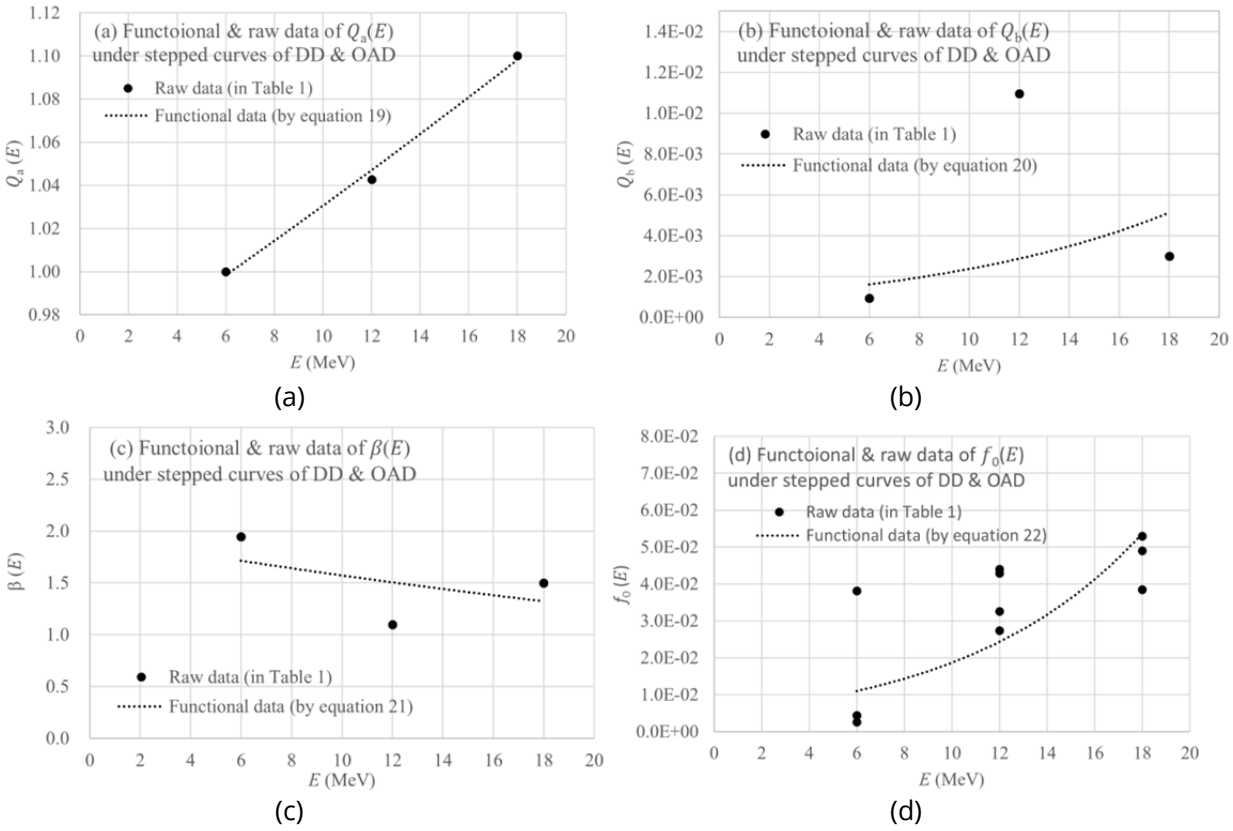

Figure A1 Diagrams showing how the regression functions of equations 19-22, which are respectively constructed for (a) $Q_{\mathrm{a}}(E)$, (b) $Q_{\mathrm{b}}(E)$, (c) $\beta(E)$, and (d) $f_0(E)$, vary with E. Each set of dots is constructed by picking up the respective data from Case-1 to -16 in Tables 1(a) and (b).

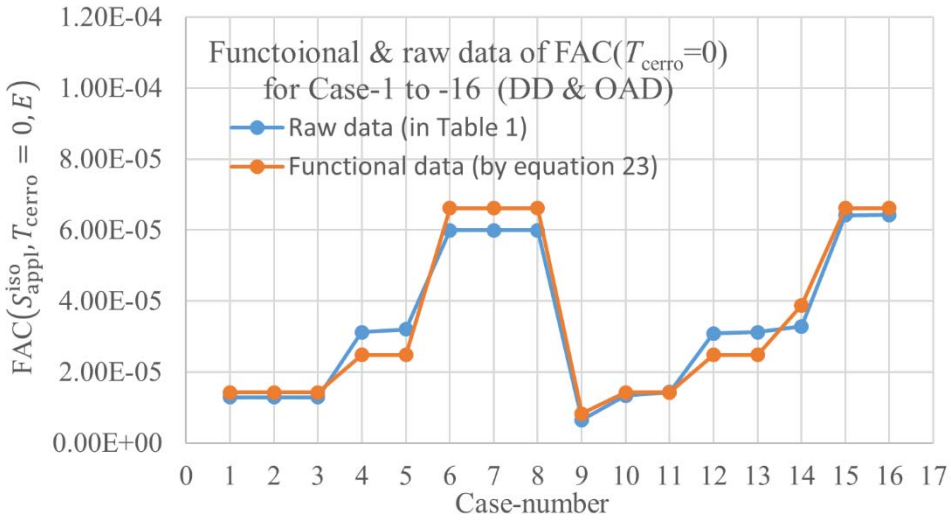

Figure A2 Diagram showing how the $\mathrm{FAC}(S^{\mathrm{iso}}_{\mathrm{appl}}, T_{\mathrm{cerro}} = 0, E)$ function of equation 23 varies for Case-1 to -16, by comparing with the corresponding data in Tables 1(a) and 1(b).

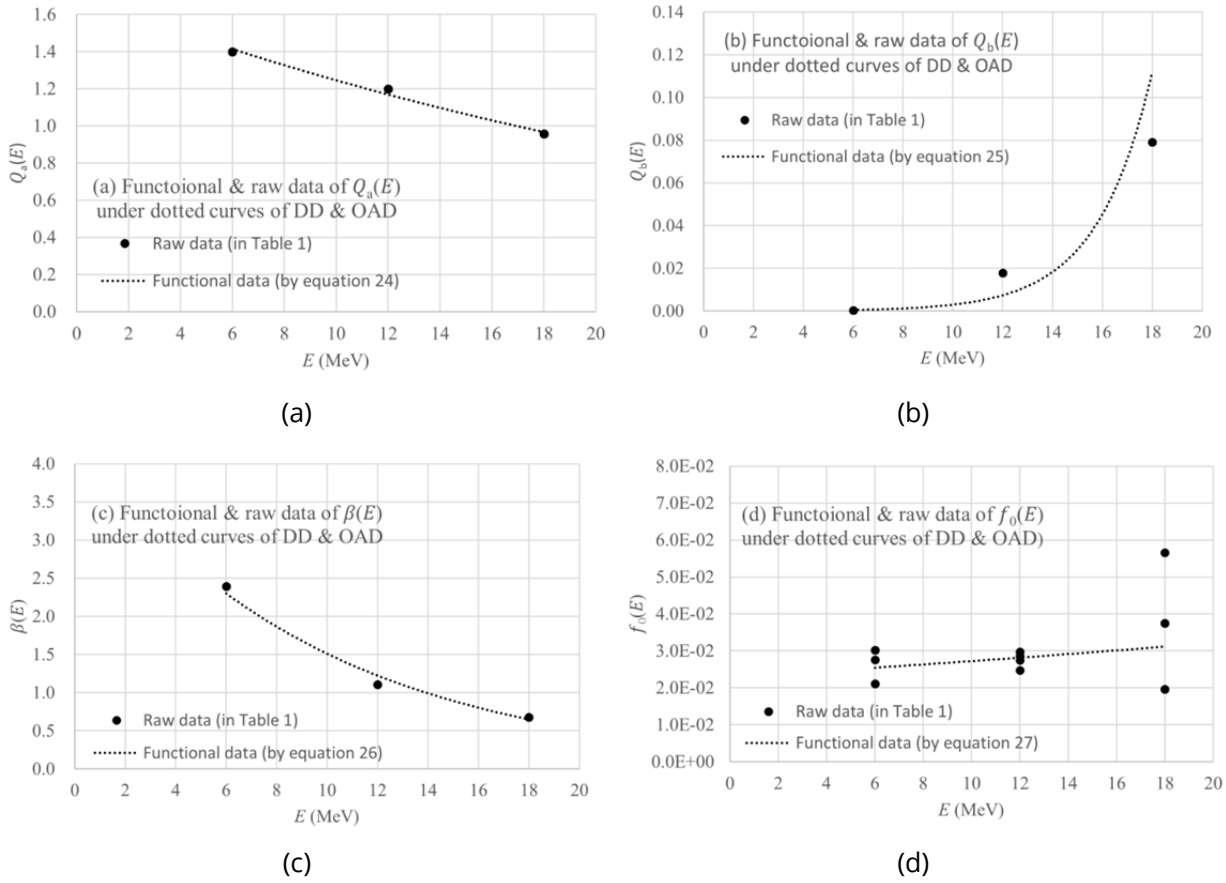

(a) (b)

(c) (d)

Figure A3 Diagrams showing how the regression functions of equations 24-27, which are respectively constructed for (a) $Q_a(E)$, (b) $Q_b(E)$, (c) $\beta(E)$, and (d) $f_0(E)$, vary with E. Each set of dots is constructed by picking up the respective data from Case-17 to -32 in Tables 1(c) and 1(d).

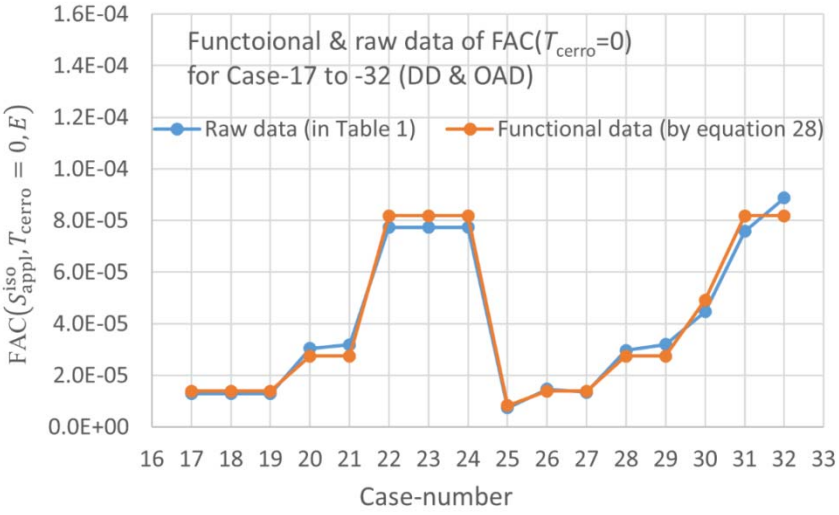

Figure A4 Diagram showing how the $\mathrm{FAC}(S^{\mathrm{iso}}_{\mathrm{appl}}, T_{\mathrm{cerro}} = 0, E)$ function of equation 28 varies for Case-17 to -32, by comparing with the corresponding data in Tables 1(c) and (d).

Appendix B

Datasets for the DD and OAD

Figure B1 illustrates calculated and MC-based DD datasets ($X_{\mathrm{cal}} = 0, Y_{\mathrm{cal}} = 0, Z_{\mathrm{cal}} =$ varied (=depths)) for Case-1 to -8 (refer to Table 1(a)). The MC-based DD datasets are illustrated using dots that are transcribed from the stepped curves of DD from the W-K MC work. The calculated DD datasets are yielded based on Clarkson's sector method described above with the functions and constants listed in Table 1(a). It can be seen that both MC-based and calculated DD datasets for each of Case-1 to -8 coincide well with each other for points at $Z_{\mathrm{cal}} < Z_{\max}(E)$ and $Z_{\mathrm{cal}} \geq Z_{\max}(E)$. Conversely, Figure B2 illustrates calculated and MC-based OAD datasets (X_{cal} =varied (=off-axis positions), $Y_{\mathrm{cal}} = 0, Z_{\mathrm{cal}}$ =const. (=1, 2, 3, 5, 10 or 15 cm)) for Case-9 to -16 (refer to Table 1(b)). The MC-based OAD datasets are illustrated using dots that are transcribed from the stepped curves of OAD from the W-K MC work. The calculated OAD datasets are yielded based on Clarkson's sector method described above with the functions and constants listed in Table 1(b). It can be seen that the calculation cannot be accurately performed around the borders of the applicator and the cerrobend area.

Figure B3 illustrates calculated and MC-based DD datasets ($X_{\mathrm{cal}} = 0, Y_{\mathrm{cal}} = 0, Z_{\mathrm{cal}} =$ varied (=depths)) for Case-17 to -24 (refer to Table 1(c)). The MC-based DD datasets are illustrated using dots that are transcribed from the dotted curves of DD from the W-K MC work. The calculated DD datasets are yielded based on Clarkson's sector method described above with the functions and constants listed in Table 1(c). It can be seen that both calculated and MC-based DD datasets for each of Case-17 to -24 coincide well with each other for points at $Z_{\mathrm{cal}} < Z_{\max}(E)$ and $Z_{\mathrm{cal}} \geq Z_{\max}(E)$, having almost the same degree of coincidence as that shown in Figure B1. Conversely, Figure B4 illustrates calculated and MC-based OAD datasets (X_{cal} =varied (=off-axis positions), $Y_{\mathrm{cal}} = 0$, Z_{cal} =const. (=1, 2, 3, 5, 10 or 15 cm)) for Case-25 to -32 (refer to Table 1(d)). The MC-based OAD datasets are illustrated using dots that are transcribed from the dotted curves of OAD from the W-K MC work. The calculated OAD datasets are yielded based on Clarkson's sector method described above with the functions and constants listed in Table 1(d). It should be emphasized that the MC-based OAD datasets do not show such specific dose variations as shown in Figure B2 around the borders of the applicator and the cerrobend area, and that both calculated and MC-based OAD datasets for each of the irradiation conditions coincide well with each other. In particular we would like to emphasize that the present analytical dose calculation method can yield almost the same results as those provided by the MC-based dose calculation algorithm in a commercial TPS.

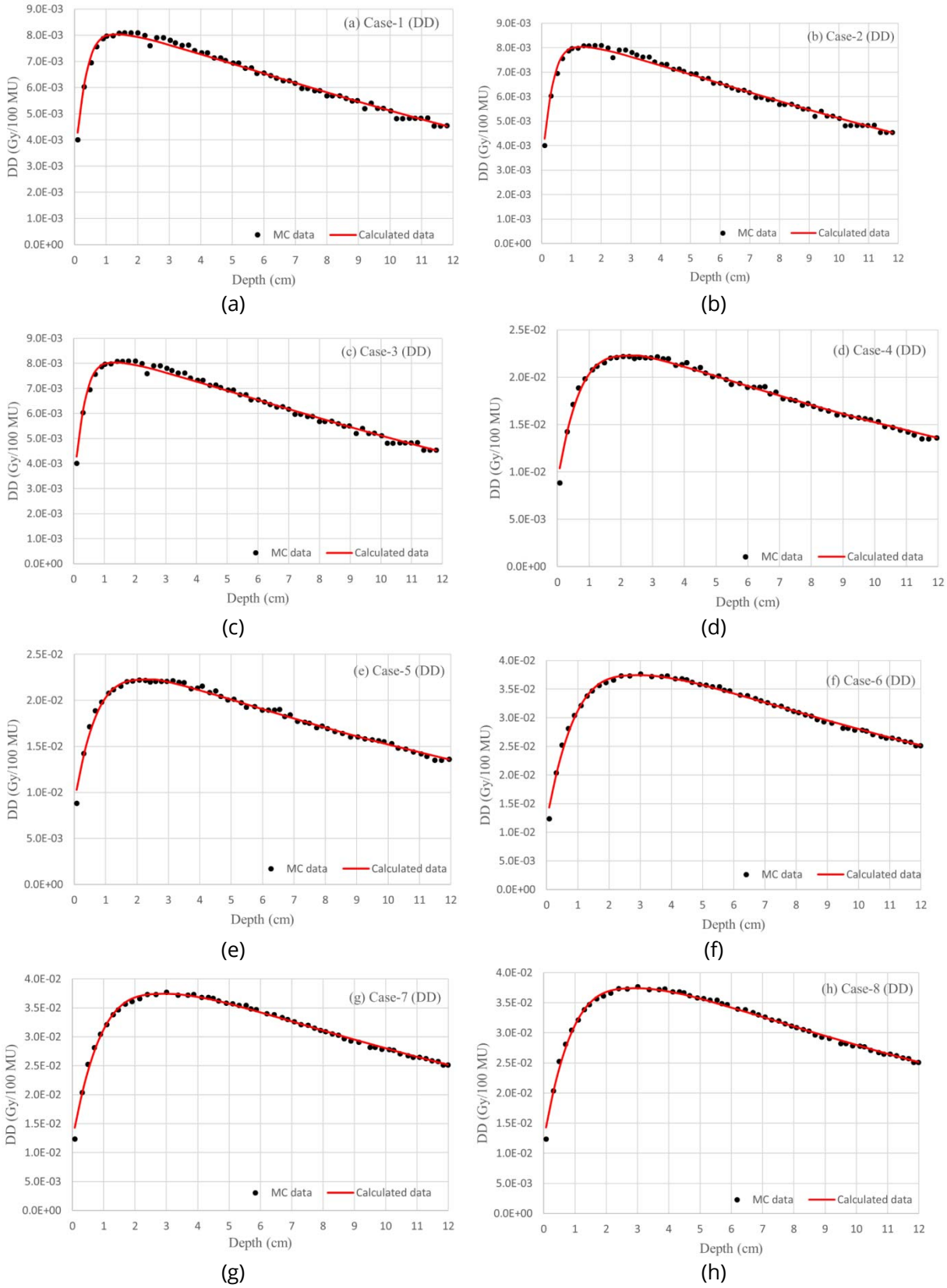

Figure B1 Two datasets of DD for each of (a) Case-1 to (h) Case-8. The solid curve is calculated, and the set of dots expresses the corresponding data from the W-K MC dose work.

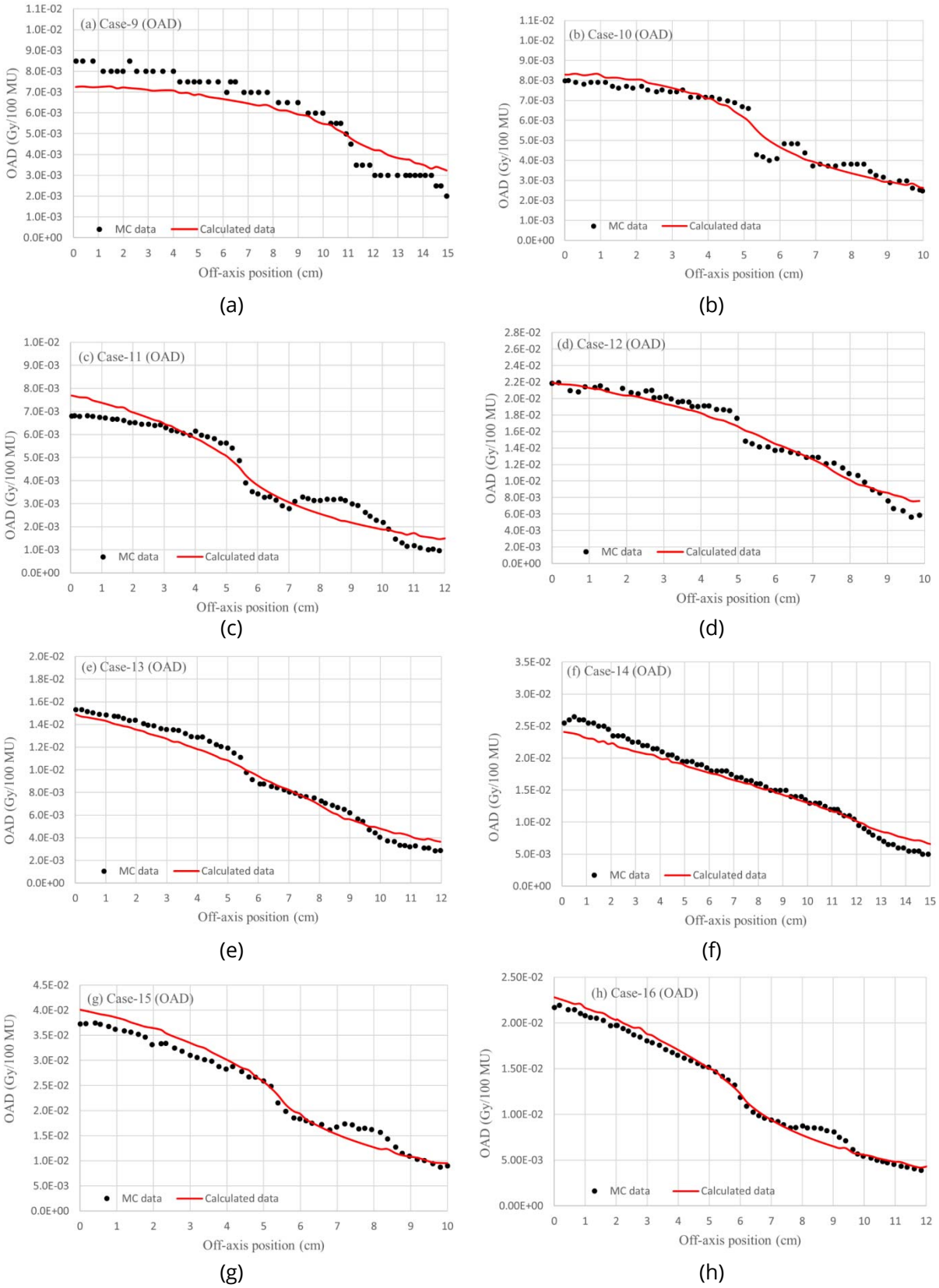

Figure B2 Two datasets of OAD for each of (a) Case-9 to (h) Case-16. The solid curve is calculated, and the set of dots expresses the corresponding data from the W-K MC dose work.

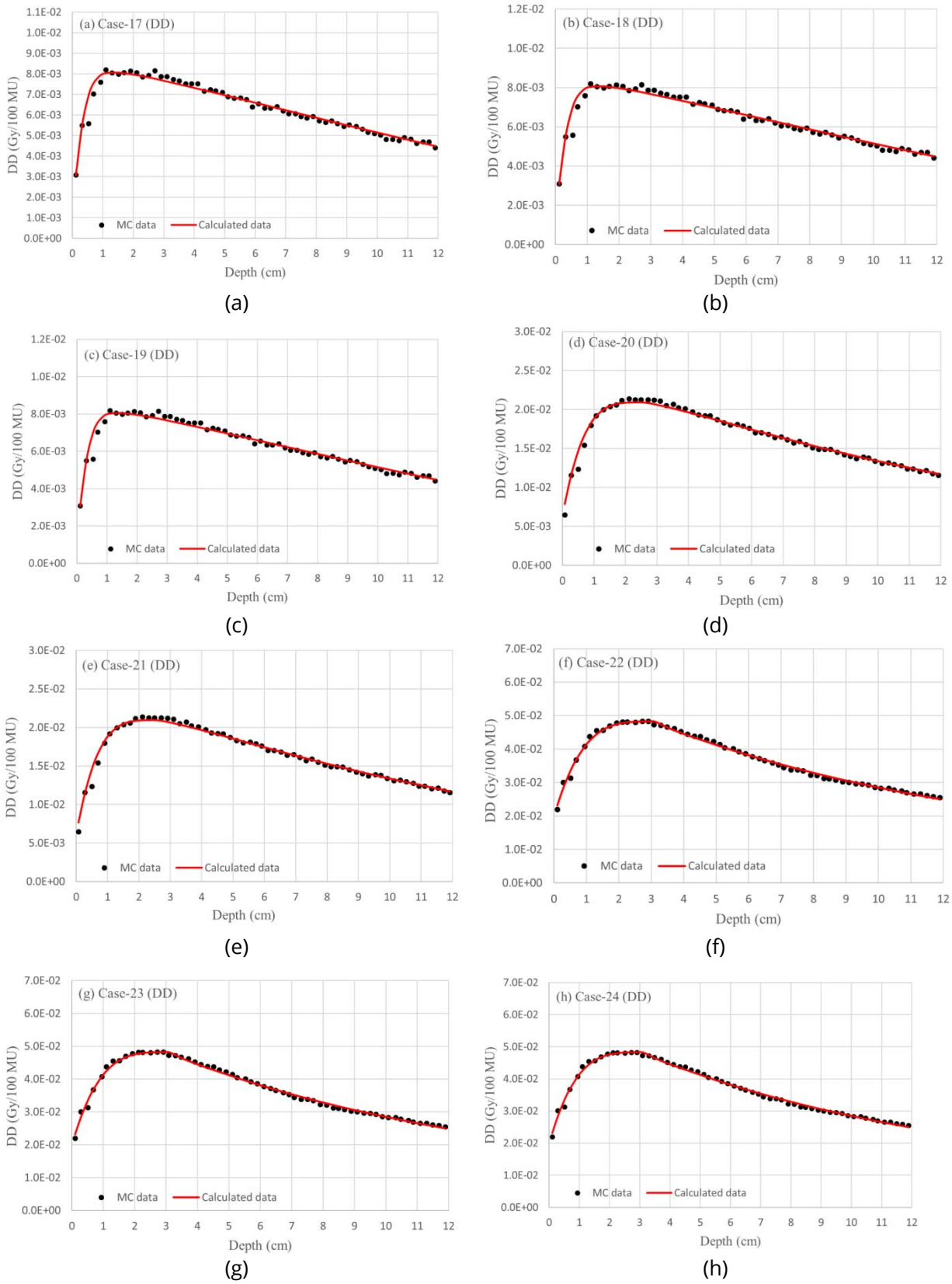

Figure B3 Two datasets of DD for each of (a) Case-17 to (h) Case-24. The solid curve is calculated, and the set of dots expresses the corresponding data from the W-K MC dose work.

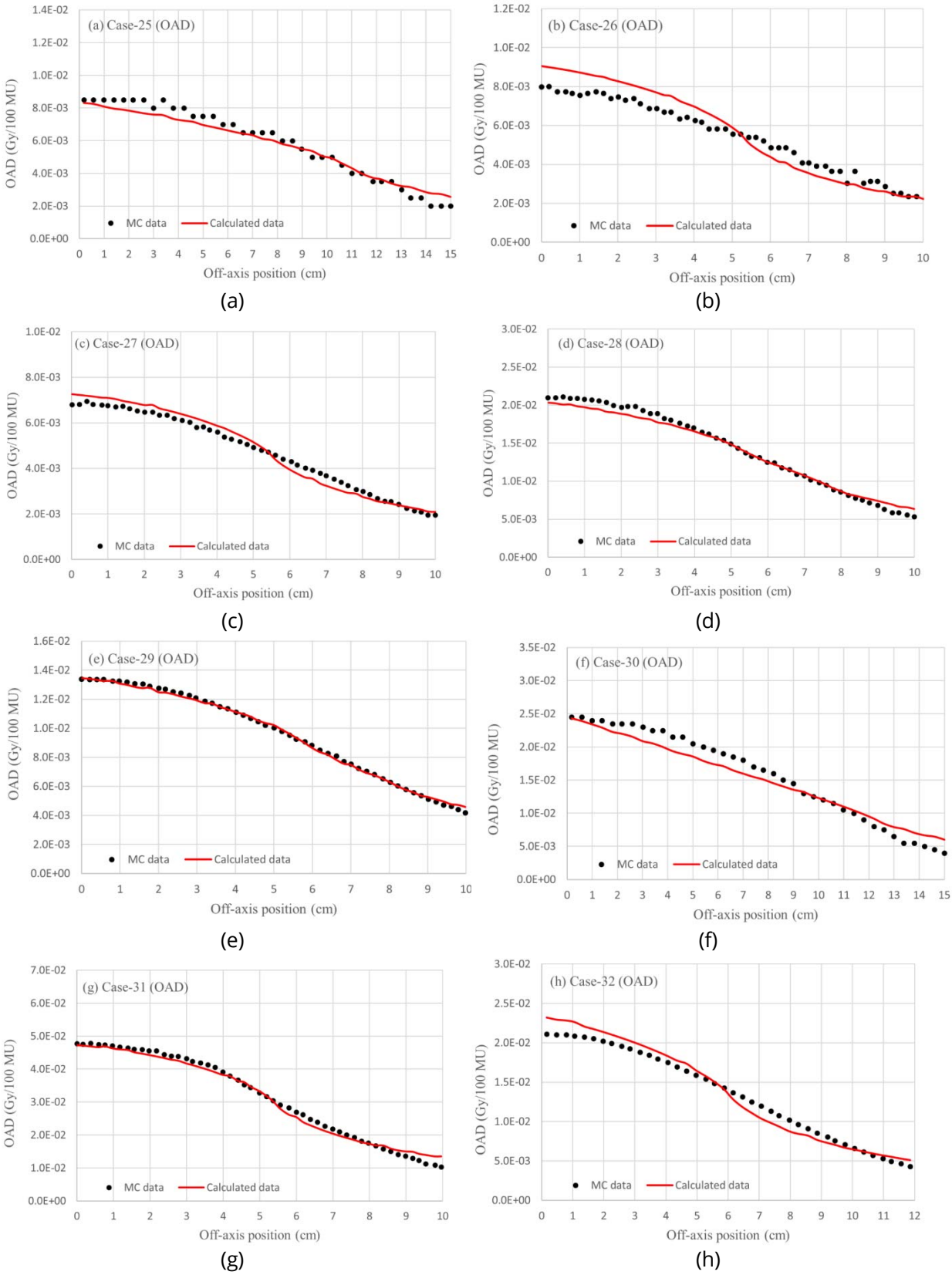

Figure B4 Two datasets of OAD for each of (a) Case-25 to (h) Case-32. The solid curve is calculated, and the set of dots expresses the corresponding data from the W-K MC dose work.

Appendix C

Datasets for the (E) function

Figure C1 illustrates how the function (E) for E=12 MeV gives effects for each of (a) Case-5 (DD) and (b) Case-13 (OAD). The solid curves are calculated using (E)=0, 0.2, 0.4, 0.6, 0.8, 0.9,1, 1.1, and 1.2 with the corresponding datasets of Case-5 and Case-13 in Table 1. The dotted sets of DD and OAD express the MC-based datasets of the W-K MC work. It should be noted that the present paper recommends α(E)=1 for analytical dose calculations, and the original sector method is performed by setting α(E)=0 as a result. As described earlier, it has been found that the value of α(E)=0 can never perform accurate dose calculation around the vague beam-field margins yielded when using the dual-foil systems. This evidence is clearly illustrated in the OAD curve (Case-13) of α(E)=0 around both margins of the electron applicator and the cerrobend area.

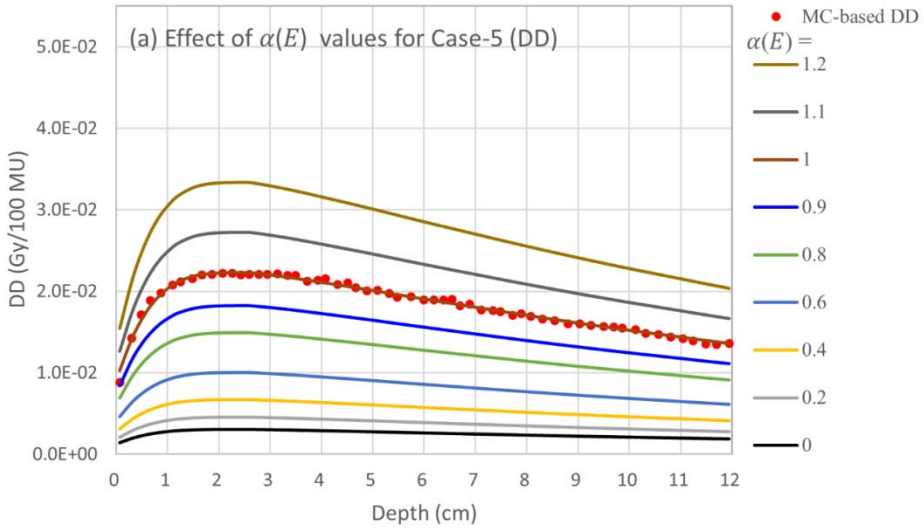

(a)

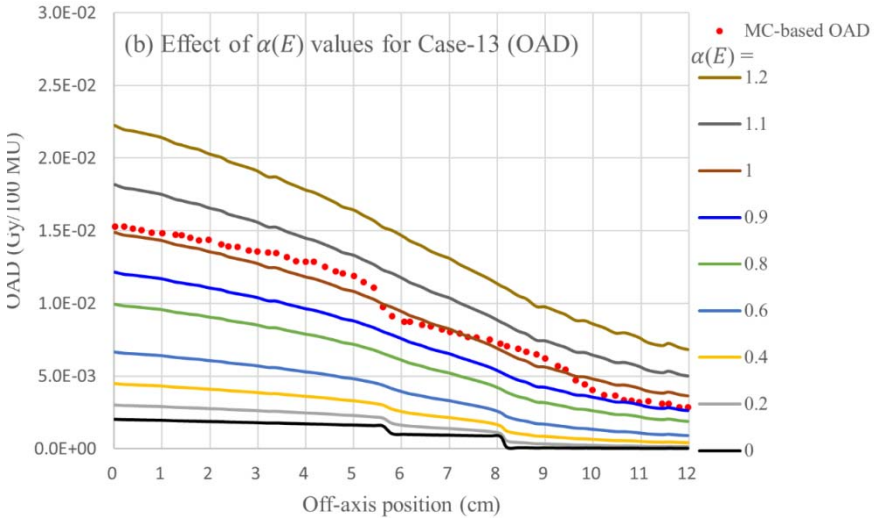

(b)

Figure C1 Diagrams showing how α(E) for E=12 MeV affects (a) Case-5 (DD) and (b) Case-13 (OAD). The sets of solid curves are calculated using α(E)=0, 0.2, 0.4, 0.6, 0.8, 0.9,1.0, 1.1, and 1.2. The sets of dots express the corresponding data from the W-K MC dose work (the present paper recommends using α(E)=1 for any E).